

Perspective on real-space nanophotonic field manipulation using non-perturbative light-matter coupling

ERIKA CORTESE¹, JOSHUA MORNHINWEG², RUPERT HUBER², CHRISTOPH LANGE³, AND SIMONE DE LIBERATO^{1,*}

¹*School of Physics and Astronomy, University of Southampton, Southampton, SO17 1BJ, United Kingdom*

²*Department of Physics, University of Regensburg, 93040 Regensburg, Germany*

³*Department of Physics, TU Dortmund University, 44227 Dortmund, Germany*

* *Corresponding author: s.de-liberato@soton.ac.uk*

Compiled November 8, 2022

The achievement of large values of the light-matter coupling in nanoengineered photonic structures can lead to multiple photonic resonances contributing to the final properties of the same hybrid polariton mode. We develop a general theory describing multi-mode light-matter coupling in systems of reduced dimensionality and we explore their novel phenomenology, validating our theory's predictions against numerical electromagnetic simulations. On the one hand, we characterise the spectral features linked with the multi-mode nature of the polaritons. On the other hand, we show how the interference between different photonic resonances can modify the real-space shape of the electromagnetic field associated with each polariton mode. We argue that the possibility of engineering nanophotonic resonators to maximise the multi-mode mixing, and to alter the polariton modes via applied external fields, could allow for the dynamical real-space tailoring of subwavelength electromagnetic fields. © 2022 Optica Publishing Group

<http://dx.doi.org/10.1364/ao.XX.XXXXXX>

1. INTRODUCTION

1 Confining light below the Abbe diffraction limit [1] by storing a
2 part of the electromagnetic energy in the kinetic energy of elec-
3 tric charges [2] opened the door to a number of groundbreaking
4 real-world applications which has contributed to the great suc-
5 cess of the field of nanophotonics. In a nanophotonic device, the
6 high energy density of the electromagnetic field makes it rela-
7 tively easy to couple with different kinds of localised material
8 excitations and reach the strong light-matter coupling regime,
9 originally achieved in cavity quantum electrodynamics (CQED)
10 atomic systems [3]. In such a regime, light and matter degrees
11 of freedom hybridise, leading to novel, polaritonic excitations of
12 mixed light-matter character [4, 5].

14 Standard theoretical models used to describe strong coupling
15 consider a single optically active matter transition coupled to
16 a single photonic mode. Although some care has to be used
17 when performing calculations on such a reduced Hilbert space
18 [6–9], this single-mode approximation has enabled modelling
19 of a wide range of CQED systems with remarkable easiness
20 and generality. However, the requirement is that the energy
21 spacing between the considered resonances and the neglected
22 ones is much larger than the strength of light-matter coupling,
23 thus permitting to integrate out excited modes with negligible

24 populations.

25 However, the ongoing race for record coupling strengths
26 [10, 11] has led to situations in which higher-energy electronic
27 states cannot be neglected, requiring a model which considers
28 the coupling of multiple matter excitations to the same photonic
29 mode. We refer to this regime as the very-strong coupling (VSC)
30 regime, first predicted by Khurgin in 2001 [12]. The hybridiza-
31 tion of multiple excited matter states has an important conse-
32 quence: the matter component of the polariton, represented itself
33 by a linear superposition of different bare matter wavefunctions,
34 has a wavefunction different from each of the bare states [13].
35 Following a 2013 proposal [14], such an effect was observed for
36 the first time in 2017 [15], as a modification of approximately
37 30% of the Wannier exciton Bohr radius in GaAs microcavities,
38 and it has been then the object of further theoretical investiga-
39 tions which confirmed the findings [16, 17]. Larger numbers of
40 matter states which can be hybridised by the coupling with the
41 photonic field could correspond to a broader design space for
42 the resulting electronic wavefunction. This idea led to the study
43 of systems with a continuum of ionised excitations [18, 19] and
44 eventually to the discovery of novel bound excitons stabilised
45 by the photonic interaction [20], and to novel polaritonic loss
46 channels [21].

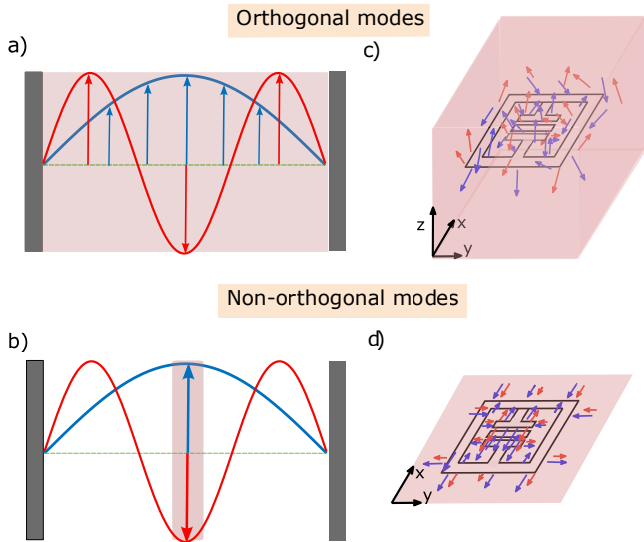


Fig. 1. Sketch of how orthogonal resonator modes can become non-orthogonal when coupled over an active region occupying only part of the resonator volume. Shown are the case of a planar microcavity (a,b) and a split-ring resonator (c,d). Two electromagnetic modes are shown by red and blue arrows, and the active region, corresponding to the full three-dimensional volume (a,c) or a thin, quasi-two-dimensional surface (b,d) is shaded in light red.

In this Article we theoretically investigate the possibility of both multi-mode electronic as well as multi-mode photonic hybridization, leading to a modification of the spatial electromagnetic profiles of the resulting polariton modes. Given the possibility of fast [22, 23] in-situ tuning of the light-matter interaction by optical and electrical means, subcycle multiwave mixing nonlinearities between different polariton states [24] or even all-optical subcycle switching [25, 26], such an approach could open the door to dynamical manipulation of subwavelength fields, with potential disruptive applications for, e.g., on-chip optical tweezers [27].

Although to the best of our knowledge it was never explicitly discussed in these terms, the regime of photonic VSC has been already described for cold atoms trapped in an optical lattice [28] and reached in various systems, as superconducting qubits coupled to microwave photons in a long transmission-line resonator [29, 30]. Moreover, it has been theoretically [31] and experimentally [32] demonstrated in microcavities, where the coupling strength becomes larger than the bare excitation frequencies. In such a regime, the diamagnetic term of the Hamiltonian creates a dominant real-space repulsive interaction localised at the dipole position, which expels the electromagnetic field and may even lead to light-matter decoupling [31, 32]. It has also been experimentally observed that, in plasmonic nanocavities, the greatly enhanced coupling between molecular excitons and gap plasmons causes a significant modification of the plasmonic modes profile [33].

Here we focus on Landau polaritons, where the giant electronic dipoles of cyclotron resonances (CRs) of two-dimensional electron gases (2DEGs) are coupled to strongly enhanced light fields of subwavelength THz resonators. After initial predictions in Ref. [34], multiple experimental realizations followed, some

of which established world-records for the largest light-matter coupling ever achieved in any CQED system [32, 35–37].

In the first part of the paper we will develop a theory describing multi-mode light-matter strong coupling in CQED. Although the theory is completely general and can be applied to arbitrary polaritonic platforms, for the sake of concreteness we specialise it to the case of Landau polaritons on which we will test it. Our approach highlights the main electronic and optical features observable for this multi-mode coupling. In the second part, we apply our formalism to structures based on planar plasmonic metasurfaces. To this end, we perform numerical simulations using a commercial finite element method (FEM) software. These simulations verify the predictions of our theory and demonstrate how multi-mode photonic hybridization can lead to a modification of the electromagnetic spatial profile of the polariton modes.

2. THEORY OF MULTI-MODE LIGHT-MATTER COUPLING

In this section we develop a theory for the light-matter coupling between M photonic resonator modes and the CRs of a 2DEG with a charge carrier density $N_{2\text{DEG}}$ and an effective mass m^* . Following Kohn's theorem [38], we neglect Coulomb interactions between the electrons, which manifest in the nonlinear susceptibility of strongly driven Landau electron systems [39], but have no role in the determination of the optical resonances. Moreover, while our theory technically describes a single quantum well (QW) hosting the entire electron distribution, it is equally valid in densely packed multi-QW structures as usually employed in experiments, where the intensity of the electromagnetic field doesn't vary significantly within the thickness of the multi-QW stack. Following the elegant theory from Ref. [37] we can write the Hamiltonian of our system as

$$\hat{H} = \hat{H}_{\text{cav}} + \sum_{j=1}^N \hbar\omega_c \hat{c}_j^\dagger \hat{c}_j + \frac{e^2}{m^*} \sum_{j=1}^N \hat{A}_-(\mathbf{r}_j) \hat{A}_+(\mathbf{r}_j) + i\sqrt{\frac{\hbar\omega_c e^2}{m^*}} \sum_{j=1}^N [\hat{c}_j^\dagger \hat{A}_+(\mathbf{r}_j) - \hat{c}_j \hat{A}_-(\mathbf{r}_j)], \quad (1)$$

where \hat{c}_j is the bosonic lowering operator for the electrons, leading to a transition from the j th to the $(j-1)$ th Landau level with a transition energy $\hbar\omega_c$, and \hat{H}_{cav} is the Hamiltonian describing the bare electromagnetic field in the resonator. In case of high electron density and strong in-plane confinement of both the 2DEG and the electromagnetic field, plasmonic modes hosted by the system can be non-negligible and lead to the formation of magneto-plasmon modes with a renormalized frequency of $\tilde{\omega}_c = \sqrt{\omega_c^2 + \omega_p^2}$, where ω_p is the 2D plasmon frequency for the 2DEG [21]. However, a correct estimation of ω_p not only takes into account the in-plane confinement of the 2DEG, but also includes the screening of the metallic resonator in proximity of the electrons, leading to a reduction of the plasmon energy [40–42]. For our structures, this effect strongly limits the extent of renormalization such that we disregard plasmon effects.

In Eq. (1) we introduced the non-Hermitian vector potentials written in terms of the in-plane component of the vector potential $\hat{\mathbf{A}}(\mathbf{r})$ as

$$\hat{A}_\pm(\mathbf{r}) = \frac{\hat{A}_x(\mathbf{r}) \mp i\hat{A}_y(\mathbf{r})}{\sqrt{2}}. \quad (2)$$

The full vector potential can be expressed as a sum of photonic modes with dimensionless spatial field profiles $\mathbf{f}_i(\mathbf{r})$, fre-

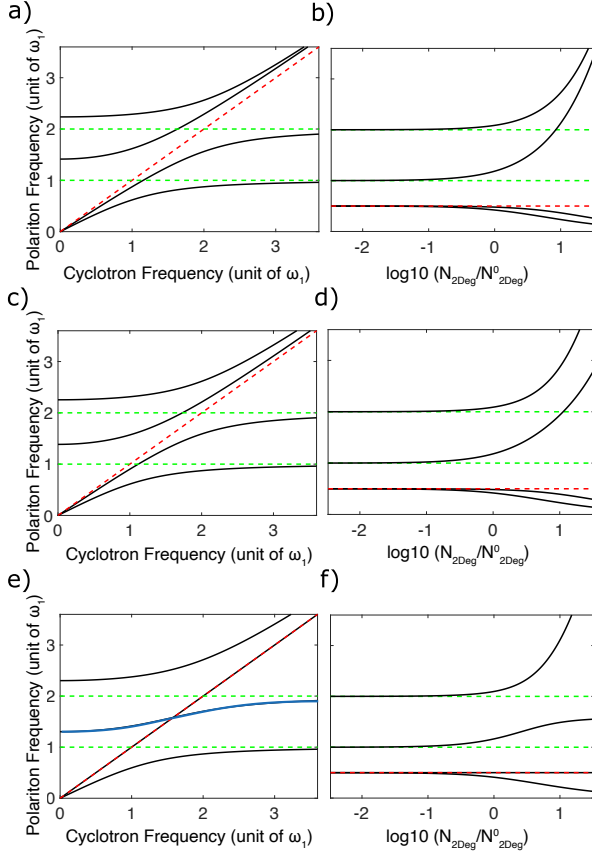


Fig. 2. Polaritonic eigenmodes arising from the diagonalization of Eq. 13 with $M = 2$ photonic resonances of frequencies ω_1 and $\omega_2 = 2\omega_1$ (green dashed lines) coupled to the 2DEG hosting the cyclotron resonance, ω_c (red dashed line). The three rows correspond to the case of zero overlap between the two photonic modes ($\eta_{2,1} = 0$; a,b), medium overlap ($\eta_{2,1} = 0.5$; c,d), or perfect overlap ($\eta_{2,1} = 1$; e,f). Panels on the left column (a,c,e) are shown as a function of the cyclotron frequency ω_c with resonant couplings in the zero overlap case ($\eta_{2,1} = 0$) $g_{1,1} = 0.5\hbar\omega_1$ at $\omega_c = \omega_1$ and $g_{2,2} = 0.25\hbar\omega_2$ at $\omega_c = \omega_2$. Panels on the right column (b,d,f) are shown for a fixed value of the cyclotron frequency $\omega_c = 0.5\omega_1$ as a function of the electron density $N_{2\text{DEG}}$. The reference density $N_{2\text{DEG}}^0$ corresponds to resonant couplings on the left column. Panel (e) displays a *S-shaped* polariton curve (blue solid line) due to a perfect overlap.

130 frequencies ω_ν , and second-quantized bosonic annihilation opera-
131 tors \hat{a}_ν as

$$\hat{\mathbf{A}}(\mathbf{r}) = \sum_\nu \sqrt{\frac{\hbar}{2\epsilon_0\epsilon_r(\mathbf{r})\omega_\nu\mathcal{V}_\nu}} \mathbf{f}_\nu(\mathbf{r}) (\hat{a}_\nu^\dagger + \hat{a}_\nu). \quad (3)$$

132 Here, the vector fields $\mathbf{f}_\nu(\mathbf{r})$ are eigensolutions of the Maxwell's
133 equations for the bare cavity, and they are thus orthogonal over
134 the full domain \mathbb{V} [43]

$$\int_{\mathbb{V}} \mathbf{f}_\nu^*(\mathbf{r}) \mathbf{f}_\mu(\mathbf{r}) d\mathbf{r} = \mathcal{V}_\nu \delta_{\nu,\mu}, \quad (4)$$

135 with \mathcal{V}_ν the mode volume of the ν th photon mode and $\epsilon_r(\mathbf{r})$ the
136 background, non-resonant dielectric constant. The amplitudes
137 of the non-Hermitian vector potentials then take the form

$$\begin{aligned} \hat{A}_-(\mathbf{r}) &= \sum_\nu \sqrt{\frac{\hbar}{2\epsilon_0\epsilon_r(\mathbf{r})\omega_\nu\mathcal{V}_\nu}} f_\nu(\mathbf{r}) (\hat{a}_\nu^\dagger + \hat{a}_\nu), \\ \hat{A}_+(\mathbf{r}) &= \sum_\nu \sqrt{\frac{\hbar}{2\epsilon_0\epsilon_r(\mathbf{r})\omega_\nu\mathcal{V}_\nu}} f_\nu^*(\mathbf{r}) (\hat{a}_\nu^\dagger + \hat{a}_\nu), \end{aligned} \quad (5)$$

138 with

$$f_\nu(\mathbf{r}) = \frac{f_{\nu,x}(\mathbf{r}) + if_{\nu,y}(\mathbf{r})}{\sqrt{2}}. \quad (6)$$

139 Crucially, the orthogonality condition in Eq. (4) holds only if
140 the integral is performed over the entire three-dimensional space,
141 while the integral of two orthogonal modes over any sub-domain
142 does not vanish in general. This concept is illustrated in Fig. 1 for
143 the model case of a planar microcavity (a,b) and for a split-ring
144 resonator (c,d), integrated over either the full three-dimensional
145 volume (a,c) or a thin, quasi-two-dimensional surface (b,d). In
146 both cases, two orthogonal modes (red and blue arrows) become
147 non-orthogonal when the integral is performed over a quasi-two-
148 dimensional slice of the overall volume. In order to understand
149 how this finding is relevant for our systems, we can consider as
150 an example the third term of Eq. (1), the so-called diamagnetic
151 term of the light-matter interaction Hamiltonian, which contains
152 generally non-vanishing expressions of the form

$$\sum_{j=1}^N f_\nu^*(\mathbf{r}_j) f_\mu(\mathbf{r}_j) = N_{2\text{DEG}} \int_S f_\nu^*(z, \mathbf{r}_\parallel) f_\mu(z, \mathbf{r}_\parallel) d\mathbf{r}_\parallel, \quad (7)$$

153 where S is the sample surface, z is the out-of-plane position
154 of the 2DEG and \mathbf{r}_\parallel is the in-plane position. Placing a 2DEG
155 at the center of the planar microcavity, or below the split-ring
156 resonator, will thus result in an interaction of different photon
157 modes which is mediated and modulated by the coupling to
158 the electrons. We now elucidate this insight further, showing
159 how it is relevant also for the dipolar light-matter interaction
160 described by the fourth term of Eq. (1). To this aim, let us call
161 M the number of photonic modes in the frequency region of
162 interest. Their wavefunctions, restricted over the sample surface
163 S , span a space of dimension at most M . We can thus always
164 introduce M orthonormal basis functions over S ,

$$\int_S \phi_\nu^*(\mathbf{r}_\parallel) \phi_\mu(\mathbf{r}_\parallel) d\mathbf{r}_\parallel = \delta_{\nu,\mu}, \quad (8)$$

165 such that,

$$f_\nu(z, \mathbf{r}_\parallel) = \sum_{\mu \leq \nu} \alpha_{\nu,\mu} \phi_\mu(\mathbf{r}_\parallel). \quad (9)$$

166 It is always possible to choose the basis such that $\alpha_{1,1}$ is real and
 167 $\alpha_{\nu,\mu} = 0$ if $\nu < \mu$. Using Eq. (9) the degree of non-orthogonality
 168 between the resonator modes with respect to the QW plane can
 169 be captured by defining the overlap matrix

$$\mathcal{F}_{\nu,\mu} = \int_{\mathcal{S}} f_{\nu}^*(z, \mathbf{r}_{\parallel}) f_{\mu}(z, \mathbf{r}_{\parallel}) d\mathbf{r}_{\parallel} = \sum_{\gamma \leq \min(\nu,\mu)} \alpha_{\nu,\gamma}^* \alpha_{\mu,\gamma}, \quad (10)$$

170 and its normalized version

$$\eta_{\nu,\mu} = \frac{\mathcal{F}_{\nu,\mu}}{\sqrt{\mathcal{F}_{\mu,\mu} \mathcal{F}_{\nu,\nu}}}, \quad (11)$$

171 both of which may assume values from 0 to 1. These matrices
 172 quantify the spatial overlap of any pair (μ, ν) of photon modes
 173 over the QW plane. A diagonal matrix $\eta_{\nu,\mu} \propto \delta_{\nu,\mu}$ implies vanishing
 174 overlap between the photon modes, while a fully populated
 175 matrix corresponds to a strong overlap.

176 By introducing a set of collective bosonic matter operators

$$\hat{b}_{\mu} = \frac{1}{\sqrt{N_{2\text{DEG}}}} \sum_{j=1}^N \phi_{\mu}(\mathbf{r}_{j,\parallel}) \hat{c}_j, \quad (12)$$

177 with the in-plane position $\mathbf{r}_{j,\parallel}$ of the j th electron, we can finally
 178 write the Hamiltonian in Coulomb Gauge as

$$\begin{aligned} \hat{H} &= \sum_{\nu} \hbar\omega_{\nu} \hat{a}_{\nu}^{\dagger} \hat{a}_{\nu} + \sum_{\nu} \hbar\omega_c \hat{b}_{\nu}^{\dagger} \hat{b}_{\nu} \\ &+ \sum_{\nu,\mu} h_{\nu,\mu} (\hat{a}_{\nu}^{\dagger} + \hat{a}_{\nu}) (\hat{a}_{\mu}^{\dagger} + \hat{a}_{\mu}) \\ &+ \sum_{\nu} \sum_{\mu \leq \nu} \left[(g_{\nu,\mu} \hat{b}_{\mu} + g_{\nu,\mu}^* \hat{b}_{\mu}^{\dagger}) (\hat{a}_{\nu}^{\dagger} + \hat{a}_{\nu}) \right]. \end{aligned} \quad (13)$$

179 Here,

$$\begin{aligned} g_{\nu,\mu} &= \alpha_{\nu,\mu} \sqrt{\frac{\hbar^2 \omega_c N_{2\text{DEG}} e^2}{2m^* \epsilon_0 \bar{\epsilon}_r \omega_{\nu} \mathcal{V}_{\nu}}}, \\ h_{\nu,\mu} &= \sum_{\gamma \leq \nu,\mu} \frac{g_{\nu,\gamma} g_{\mu,\gamma}}{\hbar\omega_c}, \end{aligned} \quad (14)$$

180 represent coupling parameters, $g_{\nu,\mu}$ is the vacuum Rabi energy
 181 quantifying the coupling between the photonic mode ν and the
 182 matter mode μ , while $h_{\nu,\mu}$ quantifies the diamagnetic coupling
 183 between two photonic modes mediated by the matter. In Eq. 14
 184 we also introduced the background dielectric constant of the QW
 185 material $\bar{\epsilon}_r$. This Hamiltonian is bosonic and quadratic, which
 186 allows us to determine its eigenmodes by Hopfield diagonaliza-
 187 tion [44]. Moreover it presents some important features. First,
 188 the light-matter interaction term displays cross-interactions be-
 189 tween different spatial modes, both in the diamagnetic term (sec-
 190 ond line of Eq. 13) and in the light-matter coupling term (third
 191 line of Eq. 13). Second, it presents so-called antiresonant terms,
 192 products of two creation or two annihilation operators. Those
 193 terms, which cannot be intuitively interpreted as describing exci-
 194 tation exchanges between different fields, become important
 195 in the ultrastrong coupling regime [10, 11]. They cannot be ne-
 196 glected when the vacuum Rabi energy becomes comparable to
 197 the energies of the bare light and matter modes, with a ratio of 0.1
 198 being usually considered the threshold to enter the ultrastrong
 199 coupling regime. Starting from such a value, the antiresonant
 200 terms have in fact led to measurable shifts in the polaritonic
 201 frequencies [45] as well as to more exotic phenomenology, as the
 202 presence of a non-negligible population of virtual excitations in
 203 the ground state [46].

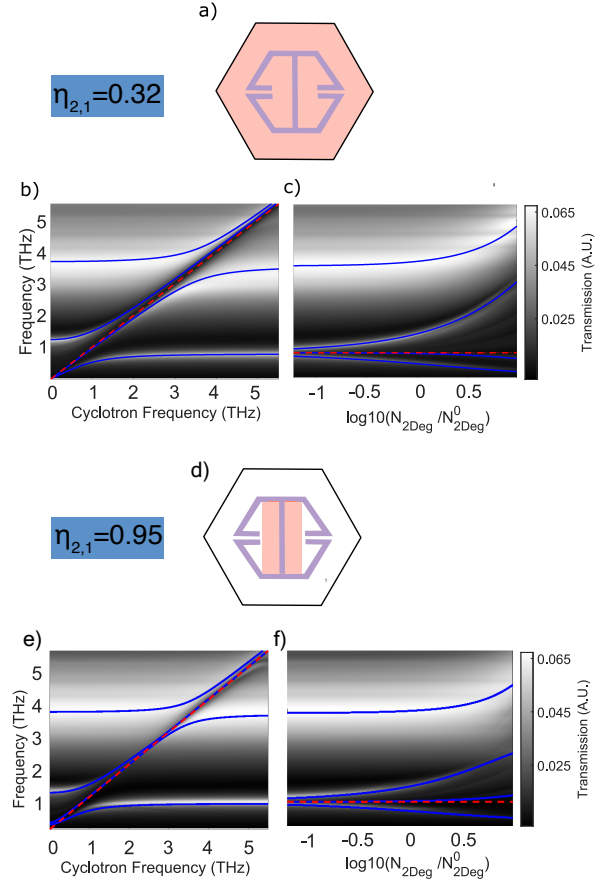


Fig. 3. Sketch of the structure including the hexagonal negative THz resonator (violet shape) fabricated on top of the GaAs substrate (white region), and the QW hosting the 2DEG (light red region), whose area occupies either the whole unit cell (a) or a limited area enclosing the central gap (d). In the other panels we show the numerical calculations of the transmission as a function of the cyclotron frequency ω_c at a fixed electron density $N_{2\text{DEG}}^0 = 3 \times 10^{12} \text{ cm}^{-2}$ (b,f) and as a function of the electron density at a fixed cyclotron frequency $\omega_c = 0.8 \text{ THz}$ (c,g). Panels (b,c) illustrate the results for the structure in panel (a), while panels (f,g) for the structure in panel (e). The calculated values of $\eta_{2,1}$ are shown in panels (a,d). Blue solid lines highlight the fitted polaritonic resonances.

Following the Hopfield approach, we diagonalise the Hamiltonian by introducing the hybrid multi-mode polariton operators,

$$\hat{p}_\mu = \sum_\nu (x_{\nu,\mu} \hat{a}_\nu + w_{\nu,\mu} \hat{b}_\nu + y_{\nu,\mu} \hat{a}_\nu^\dagger + z_{\nu,\mu} \hat{b}_\nu^\dagger), \quad (15)$$

whereby $(x_{\nu,\mu}, w_{\nu,\mu}, y_{\nu,\mu}, z_{\nu,\mu})$ are real-valued Hopfield coefficients. The dressed polariton frequencies ω_μ^p are the eigenvalues of the polariton eigenquation

$$\hbar \omega_\mu^p \hat{p}_\mu = [\hat{p}_\mu, \hat{H}]. \quad (16)$$

The Hopfield transformation can subsequently be inverted as

$$(\hat{a}_\nu + \hat{a}_\nu^\dagger) = \sum_\mu (x_{\nu,\mu} - y_{\nu,\mu}) (\hat{p}_\mu + \hat{p}_\mu^\dagger), \quad (17)$$

allowing us to find the coupled electric field components corresponding to the non-Hermitian vector potential

$$\begin{aligned} \hat{E}_-(\mathbf{r}) &= \sum_{\nu,\mu} \sqrt{\frac{\hbar \omega_\nu}{2\epsilon_0 \bar{\epsilon}_r \mathcal{V}_\nu}} f_\nu(\mathbf{r}) (x_{\nu,\mu} - y_{\nu,\mu}) (\hat{p}_\mu^\dagger + \hat{p}_\mu), \\ \hat{E}_+(\mathbf{r}) &= \sum_{\nu,\mu} \sqrt{\frac{\hbar \omega_\nu}{2\epsilon_0 \bar{\epsilon}_r \mathcal{V}_\nu}} f_\nu^*(\mathbf{r}) (x_{\nu,\mu} - y_{\nu,\mu}) (\hat{p}_\mu^\dagger + \hat{p}_\mu). \end{aligned} \quad (18)$$

From Eq. (18) we can clearly see that, as expected from our initial discussion, the electric field corresponding to the polaritonic mode \hat{p}_μ is a linear combination of all bare electromagnetic mode profiles $f_\nu(\mathbf{r})$, each weighted by the Hopfield coefficients. When the vacuum Rabi energies in Eq. 14 become comparable to the energy spacing between different resonator modes, multiple terms of such a linear combination can become non-negligible. In this case the interference of different bare electromagnetic modes weighed by the relative Hopfield coefficients can strongly modify the spatial profile of the polariton electromagnetic mode, the hallmark of photonic VSC described in the introduction.

We stress that we have developed an inherently lossless theory based on a system Hamiltonian. This model is justified because we deal with systems in which we can identify discrete, albeit broadened, independently addressable electromagnetic modes. The VSC physics is due to the interaction between the optically active material and these intra-cavity modes. Losses then only cause a Lorentzian broadening, which can be taken into account *a posteriori* using one of the perturbative schemes which have been devised for systems in the ultrastrong coupling regime [47, 48], without affecting the VSC phenomenology object of this paper. This is proven by the fact our lossless theory fits well the numerical FEM results, even if the highest photonic mode is substantially broadened. A finite linewidth can be understood as a frequency uncertainty, which translates in an uncertainty of the same order on the value of the cyclotron frequency corresponding to a specific interference figure. For such a reason, when comparing snapshots of field profiles between the lossless Hamiltonian theory and lossy FEM results, we will fit the cyclotron frequency within half of the resonance linewidth.

The opposite case, VSC with a continuum, has been achieved, both the standard electronic version [20] and the photonic one [30], and multiple approaches have been developed to study the coupling with a photonic continuum in the ultrastrong coupling regime [19, 46]. These are nevertheless not relevant for the system considered here but rather a topic for future investigations.

Note moreover that systems with structured photonic continua can be described as multiple interacting resonances [49, 50]. However, this is unrelated to the VSC effect we study here, as in such a case the interaction is a weak coupling effect between spectrally overlapping modes, independent from the coupling with the optically active material.

3. SEMI-ANALYTICAL RESULTS

In order to highlight the role of the normalised overlap factors for the coupling strength, we now assume a single pair of photonic modes ($M = 2$) with frequencies ω_1 and ω_2 and mode volumes \mathcal{V}_1 and \mathcal{V}_2 . Their non-orthogonality is quantified by a single overlap parameter $\eta_{2,1}$. By expliciting Eq. (10), we arrive at

$$\begin{aligned} \mathcal{F}_{1,1} &= \alpha_{1,1}^2, \\ \mathcal{F}_{2,2} &= |\alpha_{2,1}|^2 + |\alpha_{2,2}|^2, \\ \mathcal{F}_{2,1} &= \alpha_{2,1}^* \alpha_{1,1}, \end{aligned} \quad (19)$$

which leads to

$$\begin{aligned} \alpha_{1,1} &= \sqrt{\mathcal{F}_{1,1}}, \\ \alpha_{2,1} &= \frac{\mathcal{F}_{2,1}^*}{\sqrt{\mathcal{F}_{1,1}}} = \sqrt{\mathcal{F}_{2,2} \eta_{2,1}^*}, \\ \alpha_{2,2} &= \sqrt{\mathcal{F}_{2,2} - \frac{|\mathcal{F}_{2,1}|^2}{\mathcal{F}_{1,1}}} = \sqrt{\mathcal{F}_{2,2}} \sqrt{1 - |\eta_{2,1}|^2}. \end{aligned} \quad (20)$$

Defining the renormalised mode volume as $\tilde{\mathcal{V}}_\nu = \frac{\mathcal{V}_\nu}{\mathcal{F}_{\nu,\nu}}$, Eq. (14) leads to expressions for the coupling strengths

$$\begin{aligned} g_{1,1} &= \sqrt{\frac{\hbar^2 \omega_c N_{2\text{DEG}} e^2}{2m^* \epsilon_0 \bar{\epsilon}_r \omega_1 \tilde{\mathcal{V}}_1}}, \\ g_{2,1} &= \sqrt{\frac{\hbar^2 \omega_c N_{2\text{DEG}} e^2}{2m^* \epsilon_0 \bar{\epsilon}_r \omega_2 \tilde{\mathcal{V}}_2}} \eta_{2,1}, \\ g_{2,2} &= \sqrt{\frac{\hbar^2 \omega_c N_{2\text{DEG}} e^2}{2m^* \epsilon_0 \bar{\epsilon}_r \omega_2 \tilde{\mathcal{V}}_2}} \sqrt{1 - |\eta_{2,1}|^2}. \end{aligned} \quad (21)$$

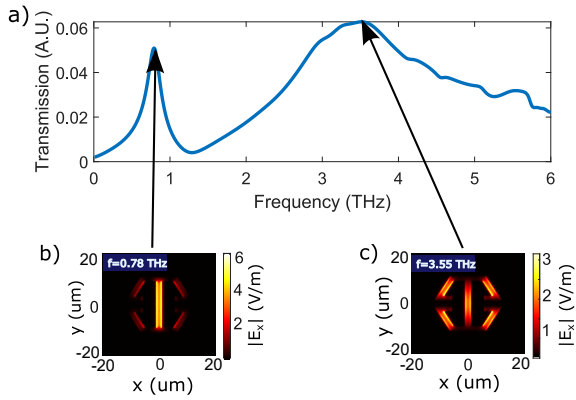
For the given basis, the interpretation of these coefficients is that the photonic mode $\nu = 1$ is coupled to only a single matter mode, $\mu = 1$. In contrast, the coupling strength for the photonic mode $\nu = 2$ originates from simultaneous coupling to both matter modes owing to the non-vanishing overlap parameter $\eta_{2,1}$.

In order to show the peculiar spectroscopic features expected in systems with non-negligible overlap between the photonic modes, we plot in Fig. 2 the spectra obtained by diagonalising the Hamiltonian in Eq. (13) for two resonator modes. The three cases concern settings of vanishing overlap ($\eta_{2,1} = 0$, panels a,b), medium overlap ($\eta_{2,1} = 0.5$, panels c,d), and maximum overlap ($\eta_{2,1} = 1$, panels e,f), whereby in each case the left and right panel show spectra as a function of the cyclotron frequency, and electron density $N_{2\text{DEG}}$, respectively.

We can point out two characteristic signatures for the overlap. First, we consider varying the cyclotron frequency (panels a,c,e). For vanishing mode overlap $\eta_{2,1} = 0$ (panel a), we observe the opening of separate polariton gaps for each pair of photonic mode and matter excitation. On the contrary, maximum overlap of $\eta_{2,1} = 1$ (panel e) leads to the emergence of a *S-shaped* resonance (blue curve). In this case, the mode structure originates from the coupling of a single matter excitation $\mu = 1$ to both

287 photonic modes $\nu = 1, 2$, simultaneously, leading to three polariton branches in total. The *S-shaped* center mode is confined
 288 between the cavity frequencies ω_1 and ω_2 , thus manifesting a
 289 double-mode nature. Second, we analyze the mode structure
 290 as a function of electron density (panels b,d,f). Here, we see
 291 that at larger densities and thus larger couplings, two modes
 292 blue-shift in the case of vanishing overlap, while a single mode
 293 blue-shifts in the presence of substantial overlap. We attribute
 294 this behavior to the contribution of the diamagnetic term which,
 295 being of higher order in $N_{2\text{DEG}}$, becomes dominant at very large
 296 densities and tends to blue-shift the upper polariton of each
 297 set of polaritonic solutions, taking into account that polaritonic
 298 modes never cross their bare components [31, 51]. Nevertheless,
 299 in the case of maximum overlap, the diamagnetic term between
 300 the two photonic modes leads to a repulsion of the upper polaritons,
 301 leading to an anti-crossing behaviour above a certain
 302 critical value of the electronic density.
 303

304 4. NUMERICAL RESULTS



305 **Fig. 4.** Transmission spectra for the resonator (a). The resonances with frequencies up to 5THz are identified by black arrows and the corresponding in plane field distribution along the gap direction is plotted for each of the $M = 2$ resonance in panel (a) with bare frequencies $\omega_1 = 0.78$ THz (b) and $\omega_2 = 3.55$ THz (c).

306 In order to explore the relevance of our theory for experiments with Landau polaritons, we used a commercial FEM software to compute the complex field distribution and transmission spectra without any fitting parameter.

307 Our structure is a *negative* resonator (cut from a gold surface, Fig. 3) [52] of hexagonal shape, fabricated on top of a gallium arsenide (GaAs) substrate (white area in panels a,d), with the cyclotron resonances hosted in 3 GaAs QWs, each doped at a density $N_{2\text{DEG}}/3$ (light red region in panels a,d), so that the total surface carrier density is $N_{2\text{DEG}}$. The approach we used to simulate the metamaterial coupled to the doped multiple QWs stack was reported by Bayer et al. [32] and we will briefly resume the main steps below.

308 To reduce the numerical complexity of modelling the dielectric environment composed of several QWs and corresponding barriers, we employ an effective medium approach describing the full QW stack as a layer of a total thickness of $d_{\text{QW}} = 210$ nm and a total surface density $N_{2\text{DEG}}$ [53]. The cyclotron resonance of the 2DEG is implemented as a gyrotropic medium, where the dielectric tensor of a plasma of charge carriers magnetically

325 biased along the z -direction describes the two-dimensional polarization response of the cyclotron resonance in the plane perpendicular to the magnetic field

$$326 \epsilon_{CR} = \begin{pmatrix} \epsilon_{xx}(\omega) & i\epsilon_{xy}(\omega) & 0 \\ -i\epsilon_{xy}(\omega) & \epsilon_{xx}(\omega) & 0 \\ 0 & 0 & \bar{\epsilon}_r \end{pmatrix}, \quad (22)$$

328 with

$$329 \epsilon_{xx}(\omega) = \bar{\epsilon}_r - \frac{\omega_{p3D}^2 (\omega + i\Gamma)}{\omega [(\omega + i\Gamma)^2 - \omega_c^2]},$$

$$330 \epsilon_{xy}(\omega) = \frac{\omega_{p3D}^2 \omega_c}{\omega [(\omega + i\Gamma)^2 - \omega_c^2]}. \quad (23)$$

331 Here, ω_{p3D} is the characteristic plasma frequency describing the oscillation of the electrons with a homogeneous 3D density $N_{2\text{DEG}}/d_{\text{QW}}$, and Γ is the phenomenological scattering rate. In the z direction we only employ the background dielectric constant, as the confinement inhibits a plasma response. For the gold metamaterial we use the dielectric constant $\epsilon_{\text{Au}} = 10^5 + 10^5 i$ [32] in order to approximate the response of a perfect metal. In the x - y -direction, we employ periodic boundary conditions to reflect the array character of our structure. Maxwell's equations are subsequently solved numerically. The transmission is derived from the electric field amplitude calculated in the far field and is expected to predict the experimental results across the entire spectral range with high accuracy.

332 In order to explore the direct impact of the overlap over the optical spectrum, we consider two types of QW designs. In the first layout the 2DEG covers the whole unit cell area (panel a). We refer to this design as *unstructured*. A second layout is instead realised by in-plane confinement of the 2DEG within a small rectangular patch at the center of the resonator (panel d). We refer to this layout as *structured*.

333 The numerical transmissions for the four samples are shown in panels (b,e) as a function of the cyclotron frequency, and in panels (c,f) as a function of the electron density $N_{2\text{DEG}}$. The simulation is performed considering an exciting electromagnetic wave which is linearly polarized along the gap (x) direction, and incident perpendicularly to the metamaterial plane. From the transmission spectrum at low electronic density, shown in Fig. 4 (a), we recognize $M = 2$ active photon resonances within the given frequency range, whose in-plane field profiles along the gap direction are plotted in Fig. 4 (b,c).

334 In the structured case the patch acts as a Fabry-Pérot resonator for the quasi-2D plasmonic excitations of the electron gas in the QWs [54]. This leads to a non-vanishing frequency for the fundamental plasmonic mode to which the lower polariton in panel (e) of Fig. 3 would converge for a vanishing cyclotron frequency. We estimated the fundamental plasmon mode frequency using the formula [40]

$$335 \omega_p^0 = \sqrt{\frac{N_{2\text{DEG}} e^2 \pi}{2m^* \epsilon_0 \epsilon_{\text{eff}} W}}, \quad (24)$$

336 with W the patch width and ϵ_{eff} the effective permittivity taking into account the screening of the gold resonator by averaging the screened and unscreened portions of the QW area. The resulting value is $\omega_p^0 \approx 0.2$ THz. Although for the sake of completeness we did use such a value in our simulations for the structured

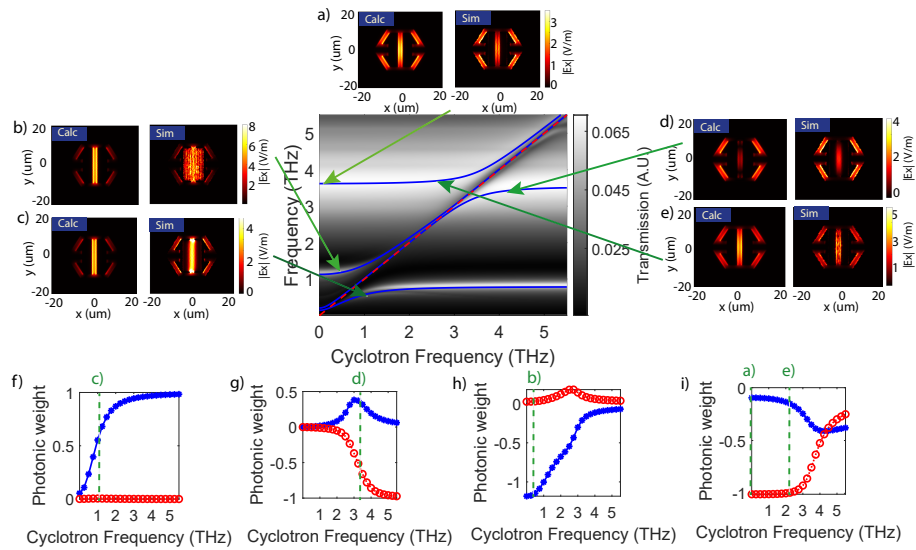


Fig. 5. Simulated Transmission spectrum as function of ω_c at $N_{2\text{DEG}} = 3 \times 10^{12} \text{ cm}^{-2}$ for the hexagonal resonator shown in Fig. 3 (d), corresponding to the overlap factor $\eta_{2,1} = 0.95$. The colormaps (a-e) represent the in-plane electric field profile along the gap direction $|E_x|$ (the y -component results negligible), extracted on the QW plane, corresponding to the coordinates marked by the green arrows. The bottom panels (f-i) display the weight $|x_{v,\mu} - y_{v,\mu}|$ of the photonic mode v in the polariton mode μ , as appearing in Eq. (18) for all the polariton modes, with the coordinates of the colormaps above marked by dashed green lines. The (f-i) plots are ordered following an ascendant order for the polariton frequencies.

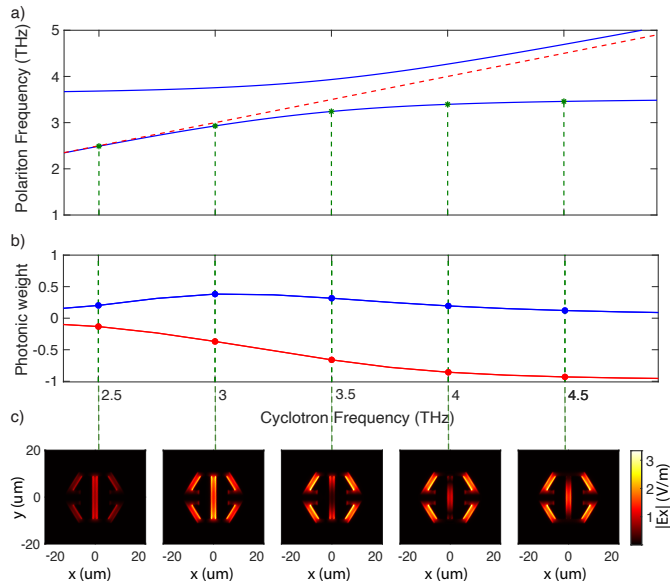


Fig. 6. Evolution of the electric field map for the second lower polariton mode. (a) Frequency dispersion for the second and fourth coupled modes (blue solid lines) as a function of the cyclotron frequency (red dashed line) at the fixed electron density $N_{2\text{DEG}} = 3 \times 10^{12} \text{ cm}^{-2}$. (b) Photonic weight components ($v = 1$ blue dotted curve, $v = 2$ red dotted curve) for the second (lower) polariton mode. (c) In-plane electric field profiles corresponding to the frequency coordinates marked by the vertical green dashed lines in (a) and (b).

364 QWs, we notice that for such low frequencies the polaritons have
 365 vanishing photonic components and the transmission spectra
 366 are not noticeably affected by the exact value of ω_p^0 .

367 Once we calculated the overlap parameter as in Eq. (11) for
 368 the two configurations, we employed our multimode theory to
 369 fit simultaneously the resonances for both the spectra of the ω_c -
 370 sweep and the $N_{2\text{DEG}}$ -sweep, considering the matter resonance
 371 as the magnetoplasmon mode $\tilde{\omega}_c$ and treating the normalised
 372 mode volumes \tilde{V}_v as fitting parameters.

373 From the discussion in the previous section we expect that
 374 passing from the unstructured to the structured sample, as the
 375 integration surface is reduced, not only the normalised mode
 376 volumes \tilde{V}_v will vary, but also the modes will become less ortho-
 377 gonal, thus increasing the overlap parameter $\eta_{2,1}$. This is indeed
 378 the case as can be seen by the calculated values of $\eta_{2,1} = 0.32$ for
 379 the unstructured sample in Fig. 3 (a) and of $\eta_{2,1} = 0.95$ for the
 380 structured sample in Fig. 3 (d) derived by Eq. (11).

381 Comparing the transmission spectra for the different config-
 382 urations allows us to recognize, albeit in attenuated form, the
 383 main differences in the spectral features predicted by the theory
 384 (marked on the plots by blue solid lines). At a first glance, we
 385 notice that the single polariton anticrossings are well resolved
 386 in the unstructured case, as they mainly arise from one-to-one
 387 coupling of photonic modes to orthogonal matter excitations. In
 388 the structured platform instead, we observe a reduction of the
 389 polariton splitting, and the appearance of a *S-shaped* resonance.
 390 The reduction of the polariton splitting is mainly due to the fact
 391 that reducing the integration area for the single mode leads to
 392 a larger normalised mode volume \tilde{V}_v , and as such to a smaller
 393 coupling strength. On the other hand, the confinement of the
 394 2DEG around the central gap of the resonator increases the over-
 395 lap between the modes, which becomes close to 1, leading to the
 396 appearance of the characteristic S-shaped polariton.

397 We report in Figs. 5 the in-plane electric field distributions
 398 along the gap direction for the coupled modes of the hexagonal

resonator platform in the structured configuration. The reported data sets are extracted from the FEM simulation and calculated by our multimode theory, respectively, and plotted at the right and left sides of panels (a-e). The simulation field maps for a given coupled mode are obtained by simulating the far-field excitation of the system at the specific value of ω_c , marked by the green arrows in the ω_c -sweep transmission plot, with excitation frequency corresponding to that of the polariton mode.

The corresponding theoretical electric field profiles are instead obtained by Eq. (18) as linear combinations of the numerically extracted fields of the uncoupled resonances, shown in Fig. 4, weighed by the photonic coefficients displayed by panels in 5 (f-i). Note that, as explained at the end of Sec. 2, the linear superposition is calculated at a cyclotron frequency fitted within half of the resonance linewidth from the nominal one. By observing the field maps we can notice that these refer to three different cases: panels (a,c,e) display field distributions similar to the uncoupled ones, as the weight of one of the two modes is greatly dominant over the other. Panel (d) displays a case in which the two photonic weights are comparable, and the electric field map is noticeably different from either of the bare ones. Finally, in panel (b) our theory predicts the field of the bare photonic mode mainly localised in the central gap, while the simulation shows the electric field diffracting in the far-field of the plasma waves, although remaining confined on the area of the QW patch. This effect is related to the one recently investigated in Ref. [21]. Here, the authors point out how the electromagnetic field, confined in the resonator gap, can excite a continuum of propagative high-wavevector plasmonic waves leaking away energy from the polaritonic resonances. In our case the main difference is that the patch acts as a Fabry-Pérot resonator. Even if higher-order discrete modes are quasi-resonant with one more polaritonic branches, the energy of the excited modes remains confined in the patch and has thus only a limited effect on the polaritonic resonances [55]. Our two-mode Hopfield model misses this effect, which could nevertheless be correctly described expanding the basis to include many discrete plasmonic modes of the patch [18] or alternatively using a theory able to deal with continuum spectra [19].

Finally, Fig. 6 highlights the modification of the in-plane electric field driven by the multi-mode hybridization for the specific case of the second polariton mode across the anticrossing point with the higher photonic frequency $\omega_2 = 3.55$ THz. The calculated electric field maps in (c) refer to the cyclotron frequency values marked by the vertical black dashed lines in panels (a) and (b) (same as Fig. 5 (g)). We can clearly see how changing the cyclotron frequency varies the electric field map, displacing the minimum of the field across the sub-wavelength central gap, a feature suggestive of potential applications in sub-wavelength sensing and optical tweezers.

Our results thus demonstrate that, by optimizing the resonator-2DEG structure, we are able to dynamically modify the sub-wavelength electromagnetic field profile, moving its maxima by varying the applied magnetic field.

5. CONCLUSIONS

In conclusion, we theoretically investigated the multi-mode coupling between the cyclotron resonances of a 2DEG and highly-confined THz-resonator modes. We developed a general theory describing multi-mode coupling taking into account the non-orthogonality of the electromagnetic modes. We highlighted specific spectral features due to the presence of multiple pho-

tonic modes and demonstrated the possibility to tune the level of inter-mode coupling by lateral confinement of the 2DEG. Finally using these effects opens up the possibility to dynamically tailor the spatial profile of sub-wavelength electromagnetic modes by varying the applied static magnetic field. This approach can potentially be used to realize sub-wavelength optical tweezers to trap and move nanoparticles over sub-micron distances.

The theoretical results encourage us to explore novel experimental methods and setups allowing to observe the predicted modification of the electric field profiles, driven by the coupling. Moreover, we aim to investigate further different resonator configurations, in order to maximise the effects of the multi-mode hybridization, heading towards novel quantum technological applications, based on a controllable and potentially dynamical tuning of high confined electromagnetic fields.

6. ACKNOWLEDGEMENTS

S.D.L. is a Royal Society Research Fellow. S.D.L. and E.C. acknowledge funding by the Leverhulme Trust (grant RPG-2022-037 and Philip Leverhulme Prize) and the Royal Society (grant RGF\EA\181001). C.L. and J.M. acknowledge funding by the DFG through Grant No. LA 3307/1-2.

7. DISCLOSURES

The authors declare no conflicts of interest.

8. DATA AVAILABILITY

The data that support the findings of this study are available from the corresponding authors on reasonable request.

REFERENCES

1. D. Ballarini and S. De Liberato, "Polaritonics: From microcavities to sub-wavelength confinement," *Nanophotonics* **8**, 641–654 (2019).
2. J. B. Khurgin, "Relative merits of phononics vs. plasmonics: the energy balance approach," *Nanophotonics* **7**, 305–316 (2018).
3. S. Haroche and J. M. Raimond, *Exploring the Quantum: Atoms, Cavities, and Photons* (Oxford Univ. Press, 2006).
4. A. Kavokin, ed., *Microcavities*, no. 16 in Series on Semiconductor Science and Technology (Oxford University Press, 2017), second edition ed.
5. D. N. Basov, A. Asenjo-Garcia, P. J. Schuck, X. Zhu, and A. Rubio, "Polariton panorama," *Nanophotonics* **10**, 549–577 (2021).
6. D. De Bernardis, P. Pilar, T. Jaako, S. De Liberato, and P. Rabl, "Breakdown of gauge invariance in ultrastrong-coupling cavity QED," *Phys. Rev. A* **98**, 053819 (2018).
7. C. Sánchez Muñoz, F. Nori, and S. De Liberato, "Resolution of superluminal signalling in non-perturbative cavity quantum electrodynamics," *Nat Commun* **9**, 1924 (2018).
8. O. Di Stefano, A. Settineri, V. Macrì, L. Garziano, R. Stassi, S. Savasta, and F. Nori, "Resolution of gauge ambiguities in ultrastrong-coupling cavity quantum electrodynamics," *Nat. Phys.* **15**, 803–808.
9. A. Stokes and A. Nazir, "Gauge ambiguities imply Jaynes-Cummings physics remains valid in ultrastrong coupling QED," *Nat Commun* **10**, 499.
10. A. F. Kockum, A. Miranowicz, S. De Liberato, S. Savasta, and F. Nori, "Ultrastrong coupling between light and matter," *Nat. Rev. Phys.* **1**, 19–40 (2019).
11. P. Forn-Díaz, L. Lamata, E. Rico, J. Kono, and E. Solano, "Ultrastrong coupling regimes of light-matter interaction," *Rev. Mod. Phys.* **91**, 025005 (2019).
12. J. Khurgin, "Excitonic radius in the cavity polariton in the regime of very strong coupling," *Solid State Commun.* **117**, 307–310 (2001).

- 518 13. J. B. Khurgin, "Pliable polaritons: Wannier exciton-plasmon coupling in 586
519 metal-semiconductor structures," *Nanophotonics* **8**, 629–639 (2019). 587
- 520 14. H. Zhang, N. Y. Kim, Y. Yamamoto, and N. Na, "Very strong coupling in 588
521 gaas-based optical microcavities," *Phys. Rev. B* **87**, 115303 (2013). 589
- 522 15. S. Brodbeck, S. De Liberato, M. Amthor, M. Klaas, M. Kamp, 590
523 L. Worschech, C. Schneider, and S. Höfling, "Experimental Verifica- 591
524 tion of the Very Strong Coupling Regime in a GaAs Quantum Well 592
525 Microcavity," *Phys. Rev. Lett.* **119**, 027401 (2017). 593
- 526 16. J. Levinsen, G. Li, and M. M. Parish, "Microscopic description of exciton- 594
527 polaritons in microcavities," *Phys. Rev. Res.* **1**, 033120 (2019). 595
- 528 17. E. Laird, F. M. Marchetti, D. K. Efimkin, M. M. Parish, and J. Levinsen, 596
529 "Rydberg exciton-polaritons in a magnetic field," *Phys. Rev. B* **106**, 597
530 125407 (2022). 598
- 531 18. E. Cortese, I. Carusotto, R. Colombelli, and S. D. Liberato, "Strong 599
532 coupling of ionizing transitions," *Optica* **6**, 354–361 (2019). 600
- 533 19. E. Cortese and S. De Liberato, "Exact solution of polaritonic systems 601
534 with arbitrary light and matter frequency-dependent losses," *The J. Chem. Phys.* **156**, 084106 (2022). 602
603
- 535 20. E. Cortese, N.-L. Tran, J.-M. Manceau, A. Bousseksou, I. Carusotto, 604
536 G. Biasiol, R. Colombelli, and S. De Liberato, "Excitons bound by 605
537 photon exchange," *Nat. Phys.* **17**, 31–35 (2021). 606
- 538 21. S. Rajabali, E. Cortese, M. Beck, S. De Liberato, J. Faist, and 607
539 G. Scalari, "Polaritonic nonlocality in light-matter interaction," *Nat. Photonics* (2021). 608
609
- 540 22. A. A. Anappara, A. Tredicucci, G. Biasiol, and L. Sorba, "Electrical 610
541 control of polariton coupling in intersubband microcavities," *Appl. Phys. Lett.* **87**, 051105 (2005). 611
- 542 23. T. Schwartz, J. A. Hutchison, C. Genet, and T. W. Ebbesen, "Reversible 612
543 switching of ultrastrong light-molecule coupling," *Phys. Rev. Lett.* **106**, 613
544 196405 (2011). 614
615
- 545 24. J. Mornhinweg, M. Halbhüser, C. Ciuti, D. Bougeard, R. Huber, and 616
546 C. Lange, "Tailored subcycle nonlinearities of ultrastrong light-matter 617
547 coupling," *Phys. Rev. Lett.* **126**, 177404 (2021). 618
- 548 25. G. Günter, A. A. Anappara, J. Hees, A. Sell, G. Biasiol, L. Sorba, 619
549 S. De Liberato, C. Ciuti, A. Tredicucci, A. Leitenstorfer, and R. Huber, 620
550 "Sub-cycle switch-on of ultrastrong light-matter interaction," *Nature* **458**, 621
551 178–181 (2009). 622
- 552 26. M. Halbhüser, J. Mornhinweg, V. Zeller, C. Ciuti, D. Bougeard, R. Huber, 623
553 and C. Lange, "Non-adiabatic stripping of a cavity field from electrons in 624
554 the deep-strong coupling regime," *Nat. Photonics* **14**, 675–679 (2020). 625
- 555 27. S. Yu, J. Lu, V. Gini, S. Kheifets, S. W. D. Lim, M. Qiu, T. Gu, J. Hu, 626
556 and F. Capasso, "On-chip optical tweezers based on freeform optics," 627
557 *Optica* **8**, 409–414 (2021). 628
- 558 28. D. Meiser and P. Meystre, "Superstrong coupling regime of cavity 629
559 quantum electrodynamics," *Phys. Rev. A* **74**, 065801 (2006). 630
- 560 29. N. M. Sundaresan, Y. Liu, D. Sadri, L. J. Szócs, D. L. Underwood, 631
561 M. Malekakhlagh, H. E. Türeci, and A. A. Houck, "Beyond strong 632
562 coupling in a multimode cavity," *Phys. Rev. X* **5**, 021035 (2015). 633
- 563 30. Y. Liu and A. A. Houck, "Quantum electrodynamics near a photonic 634
564 bandgap," *Nat. Phys.* **13**, 48–52 (2017). 635
- 565 31. S. De Liberato, "Light-Matter Decoupling in the Deep Strong Coupling 636
566 Regime: The Breakdown of the Purcell Effect," *Phys. Rev. Lett.* **112**, 637
567 016401 (2014). 638
- 568 32. A. Bayer, M. Pozimski, S. Schambeck, D. Schuh, R. Huber, 639
569 D. Bougeard, and C. Lange, "Terahertz Light-Matter Interaction beyond 640
570 Unity Coupling Strength," *Nano Lett.* **17**, 6340–6344 (2017). 641
- 571 33. X. Chen, Y.-H. Chen, J. Qin, D. Zhao, B. Ding, R. J. Blaikie, and M. Qiu, 642
572 "Mode Modification of Plasmonic Gap Resonances Induced by Strong 643
573 Coupling with Molecular Excitons," *Nano Lett.* **17**, 3246–3251 (2017). 644
- 574 34. D. Hagenmüller, S. De Liberato, and C. Ciuti, "Ultrastrong coupling 645
575 between a cavity resonator and the cyclotron transition of a two- 646
576 dimensional electron gas in the case of an integer filling factor," *Phys. Rev. B* **81**, 235303 (2010). 647
- 577 35. G. Scalari, C. Maissen, D. Turcinkova, D. Hagenmüller, S. De Liberato, 648
578 C. Ciuti, C. Reichl, D. Schuh, W. Wegscheider, M. Beck, and J. Faist, 649
579 "Ultrastrong Coupling of the Cyclotron Transition of a 2D Electron Gas 650
580 to a THz Metamaterial," *Science* **335**, 1323–1326 (2012). 651
- 581 36. G. Scalari, C. Maissen, D. Hagenmüller, S. De Liberato, C. Ciuti, C. Re- 652
582 ichl, W. Wegscheider, D. Schuh, M. Beck, and J. Faist, "Ultrastrong 653
583 light-matter coupling at terahertz frequencies with split ring resonators 654
584 and inter-landau level transitions," *J. Appl. Phys.* **113**, 136510 (2013). 655
- 585 37. X. Li, M. Bamba, Q. Zhang, S. Fallahi, G. C. Gardner, W. Gao, M. Lou, 656
586 K. Yoshioka, M. J. Manfra, and J. Kono, "Vacuum Bloch-Siegert shift 657
587 in Landau polaritons with ultra-high cooperativity," *Nat. Photon* **12**, 658
588 324–329 (2018). 659
- 589 38. W. Kohn, "Cyclotron resonance and de Haas-van Alphen oscillations of 660
590 an interacting electron gas," *Phys. Rev.* **123**, 1242 (1961). 661
- 591 39. T. Maag, A. Bayer, S. Baierl, M. Hohenleutner, T. Korn, C. Schüller, 662
592 D. Schuh, D. Bougeard, C. Lange, R. Huber, M. Mootz, J. E. Sipe, S. W. 663
593 Koch, and M. Kira, "Coherent cyclotron motion beyond Kohn's theorem," 664
594 *Nat. Phys.* **12**, 119 (2016). 665
- 595 40. V. V. Popov, O. V. Polischuk, and M. S. Shur, "Resonant excitation of 666
596 plasma oscillations in a partially gated two-dimensional electron layer," 667
597 *J. Appl. Phys.* **98**, 033510 (2005). 668
- 598 41. M. Bialek, M. Czapkiewicz, J. Wróbel, V. Umansky, and J. Łusakowski, 669
599 "Plasmon dispersions in high electron mobility terahertz detectors," *Appl. Phys. Lett.* **104**, 263514 (2014). 670
- 600 42. G. L. Paravicini-Bagliani, G. Scalari, F. Valmorra, J. Keller, C. Maissen, 671
601 M. Beck, and J. Faist, "Gate and magnetic field tunable ultrastrong 672
602 coupling between a magnetoplasmon and the optical mode of an LC 673
603 cavity," *Phys. Rev. B* **95**, 205304 (2017). 674
- 604 43. C. R. Gubbin, S. A. Maier, and S. De Liberato, "Real-space Hopfield 675
605 diagonalization of inhomogeneous dispersive media," *Phys. Rev. B* **94**, 676
606 205301 (2016). 677
- 607 44. J. J. Hopfield, "Theory of the Contribution of Excitons to the Complex 678
608 Dielectric Constant of Crystals," *Phys. Rev.* **112**, 1555–1567 (1958). 679
- 609 45. A. A. Anappara, S. De Liberato, A. Tredicucci, C. Ciuti, G. Biasiol, 680
610 L. Sorba, and F. Beltram, "Signatures of the ultrastrong light-matter 681
611 coupling regime," *Phys. Rev. B* **79**, 201303. 682
- 612 46. S. De Liberato, "Virtual photons in the ground state of a dissipative 683
613 system," *Nat. Commun.* **8**, 1465 (2017). 684
- 614 47. S. De Liberato, "Comment on 'System-environment coupling derived 685
615 by Maxwell's boundary conditions from the weak to the ultrastrong 686
616 light-matter-coupling regime'," *Phys. Rev. A* **89**, 017801 (2014). 687
- 617 48. M. Bamba and T. Ogawa, "Recipe for the Hamiltonian of system- 688
618 environment coupling applicable to the ultrastrong-light-matter- 689
619 interaction regime," *Phys. Rev. A* **89**, 023817 (2014). 690
- 620 49. S. Franke, S. Hughes, M. K. Dezfouli, P. T. Kristensen, K. Busch, 691
621 A. Knorr, and M. Richter, "Quantization of quasinormal modes for open 692
622 cavities and plasmonic cavity quantum electrodynamics," *Phys. Rev. Lett.* **122**, 213901 (2019). 693
- 623 50. I. Medina, F. J. García-Vidal, A. I. Fernández-Domínguez, and J. Faist, 694
624 "Few-mode field quantization of arbitrary electromagnetic spectral den- 695
625 sities," *Phys. Rev. Lett.* **126**, 093601 (2021). 696
- 626 51. Y. Todorov, "Dipolar quantum electrodynamics of the two-dimensional 697
627 electron gas," *Phys. Rev. B* **91**, 125409. 698
- 628 52. C. Maissen, G. Scalari, F. Valmorra, M. Beck, J. Faist, S. Cibella, 699
629 R. Leoni, C. Reichl, C. Charpentier, and W. Wegscheider, "Ultrastrong 700
630 coupling in the near field of complementary split-ring resonators," *Phys. Rev. B* **90**, 205309 (2014). 701
- 631 53. M. Zaluźny and W. Zietkowski, "Intersubband cavity polaritons: The 702
632 role of higher photonic modes," *Phys. Rev. B* **80**, 245301 (2009). 703
- 633 54. S. Das Sarma and J. J. Quinn, "Collective excitations in semiconductor 704
634 superlattices," *Phys. Rev. B* **25**, 7603–7618 (1982). 705
- 635 55. S. Rajabali, J. Enkner, E. Cortese, M. Beck, S. De Liberato, J. Faist, and 706
636 G. Scalari, "An engineered planar plasmonic reflector for polaritonic 707
637 mode confinement," to appear . 708